Squirt flow in cracks with rough walls

Simón Lissa[1], Nicolás D. Barbosa[2], Eva Caspari[3], Yury Alkhimenkov[1], Beatriz Quintal[1]

[1]Institute of Earth Sciences, University of Lausanne, Lausanne, Switzerland
[2]Department of Earth Sciences, University of Geneva, Geneva, Switzerland
[3]Chair of Applied Geophysics, Montanuniversity Leoben, Leoben, Austria

Key Points:

- We solve the quasi-static linearised Navier-Stokes equations coupled to elasticity equations.
- Seismic attenuation due to squirt-flow is strongly affected by the roughness of the crack walls.
- The minimum and the hydraulic apertures significantly affect the energy dissipation process.

Corresponding author: Simón Lissa, `simon.lissa@unil.ch`

Abstract

We explore the impact of roughness in crack walls on the P-wave modulus dispersion and attenuation caused by squirt flow. For that, we numerically simulate oscillatory relaxation tests on models having interconnected cracks with both simple and intricate aperture distributions. Their viscoelastic responses are compared with those of models containing planar cracks but having the same hydraulic aperture as the rough wall cracks. In the absence of contact areas between crack walls, we found that three apertures affect the P-wave modulus dispersion and attenuation: the arithmetic mean, minimum and hydraulic apertures. We show that the arithmetic mean of the crack apertures controls the effective P-wave modulus at the low- and high-frequency limits, thus representing the mechanical aperture. The minimum aperture of the cracks tends to dominate the energy dissipation process, and consequently, the characteristic frequency. An increase in the confining pressure is emulated by uniformly reducing the crack apertures, which allows for the occurrence of contact areas. The contact area density and distribution play a dominant role in the stiffness of the model and, in this scenario, the arithmetic mean is not representative of the mechanical aperture. On the other hand, for a low percentage of minimum aperture or in presence of contact areas, the hydraulic aperture tends to control de characteristic frequency. Analysing the local energy dissipation, we can more specifically visualise that a different aperture controls the energy dissipation process at each frequency, which means that a frequency-dependent hydraulic aperture might describe the squirt flow process in cracks with rough walls.

1 Introduction

The indirect geophysical characterisation of fluid-saturated rocks in subsurface has a fundamental role in several activities, such as the monitoring of radioactive waste disposal and of geological CO2 sequestration, the exploration and production of geothermal energy and hydrocarbons, among others (Klimentos, 1995; Rapoport et al., 2004; Metz et al., 2005; Tester et al., 2007). In particular, rock pores such as micro-cracks are very important in this scenario since they can modify significantly the hydraulic and mechanical properties of fluid-saturated rocks. Seismic methods are widely used for rock characterisation given that seismic waves are strongly affected by the presence of fluid in the rock pores as well as by the characteristics of the pore space including pore volume, compliance, distribution, and connectivity. Frequently, the porosity of rocks is split into the contributions of stiff and compliant porosities (Müller et al., 2010). Pores having spherical geometries constitute the stiff porosity often referred to as the equant porosity. Compliant porosity is represented by pores of very low aspect ratio such as microcracks and grain contacts which can be observed, for example, in micro-CT images (e.g., Andrä et al., 2013; Madonna et al., 2013). When a seismic wave propagates through a medium containing fluid saturated connected pores with different compliances, it can be significantly attenuated and dispersed due to squirt flow at the pore scale (O'Connell & Budiansky, 1977; Murphy et al., 1986; Mavko & Jizba, 1991; Dvorkin et al., 1995; Gurevich et al., 2010). In this scenario, the seismically induced pressure gradients between connected pores of dissimilar compliance are equilibrated through a fluid pressure diffusion (FPD) process. The consequent friction between particles of the viscous fluid dissipates energy. Squirt flow evidence at seismic and sonic frequencies were shown in laboratory experiments in which glycerine-saturated samples of Fontainebleau and Berea sandstones, as well as of limestones, were submitted to forced oscillations by Pimienta et al. (2015); Subramaniyan et al. (2015); Borgomano et al. (2019); S. Chapman et al. (2019).

A variety of analytical squirt flow models considering different geometries of pore shapes and cracks has been developed (e.g., O'Connell & Budiansky, 1977; Mavko & Jizba, 1991; Dvorkin et al., 1995; M. Chapman et al., 2002; Pride et al., 2004; Gurevich et al., 2010). Alkhimenkov et al. (2020) presented a comparison between numerical results and

an analytical model for squirt flow. In general, accepted analytical models should reproduce the equations of Gassmann (1951) in the low frequency limit (M. Chapman et al., 2002). The reason is that at the relaxed state for undrained boundary conditions (low-frequency limit), the time of a half period of a passing wave allows for fluid pressure to equilibrate through FPD. At the unrelaxed state (high-frequency limit), the fluid pressure has no time to equilibrate during a half period of a passing wave and the elastic properties of the saturated material are predicted by the formulation of Mavko and Jizba (1991), which assumes that no FPD occurs during the passage of the wave. At intermediate frequencies, FPD occurs inside the cracks during the passage of the wave and part of its energy is dissipated. Nevertheless, all analytical solutions assume smooth walls for the cracks despite the fact that crack walls in rocks have been observed to present complex profiles including wall roughness and contact areas, irregular shapes, among others (e.g., Pyrak-Nolte et al., 1987; Jaeger et al., 2007). In view of this limitation, numerical analyses are the most adequate tools to quantitatively explore the impact of roughness in the crack walls on squirt flow and the resulting effective moduli dispersion and attenuation.

Digital rock physics (DRP) is a technique that consists of imaging (micro-CT) and digitising the pore space, as well as, the mineral rock matrix and using numerical simulations to obtain effective rock properties, such as, elastic moduli, permeability, electrical conductivity, among others. DRP has been frequently performed with the objective of reproducing experimental measurements (e.g., Saenger et al., 2011; Dvorkin et al., 2011; Andrä et al., 2013; Saenger et al., 2016). In the particular case of elastic moduli, results obtained using DRP methods are in general not able to reproduce the corresponding laboratory observations. This is usually attributed to either the dimension of micro-cracks being below the rock image resolution (Zhang & Toksöz, 2012; Madonna et al., 2013; Das et al., 2019), or to the filters and interpreter-dependent cut-offs applied during the segmentation process (Andrä et al., 2013; Arena et al., 2014). In any case, the roughness of crack walls tends to be largely underestimated during the digitalisation process. To date, the effects of underestimating or completely neglecting the roughness of crack wall remains unexplored. Recent attempts to account for these effects include the work of Quintal et al. (2019), which considered 2-D cracks having walls with asperities producing narrow throats, and showed that a shift of the attenuation peak to lower frequencies occurs due to the change of the aperture associated with the introduced asperities. This result points to the importance of quantifying the effects of crack asperities on squirt flow and the associated seismic response.

This work focus on studying the effects of crack roughness on squirt flow in terms of the effective P-wave modulus dispersion and attenuation of a rock model. For that, we numerically perform quasi-static, oscillatory relaxation tests following the numerical scheme proposed by Quintal et al. (2016, 2019). This approach employs the quasi-static, linearised Navier-Stokes equations to describe the fluid physics within the pore space coupled with the linear elasticity equations for the solid elastic material (grains) embedding the pore space. We consider 3D models having two hydraulically interconnected micro-cracks with rough walls. In such models, cracks are perpendicularly orientated and allowing for one of them to be highly compressed during the oscillatory tests (i.e., representing the compliant porosity of the model) and the other remains nearly unaffected by the compression (i.e., representing the stiff porosity of the model). First, we consider cracks with a binary distribution of apertures (i.e., crack aperture is allowed to have only two possible values). We then extend the analysis to crack models having more intricate distributions of the crack aperture (Nolte & Pyrak-Nolte, 1991). Finally, we investigate the expected changes due to an increase in the confining pressure emulated by reducing the crack apertures and allowing for the occurrence of contact areas. We provide a comprehensive analysis of the role played by the geometrical aperture distribution as well as by the hydraulic aperture of the cracks in the numerically obtained effective moduli and attenuation.

Table 1. Material properties of the models.

Properties	Solid	Fluid
Bulk modulus K [GPa]	35	4.35
Shear modulus μ [GPa]	40	0
Fluid viscosity η [Pa · s]	0	1

2 Methodology

2.1 Mathematical formulation

We quantify the effective P-wave modulus dispersion and attenuation due to squirt flow in cracked media. For that, we numerically apply quasi-static, oscillatory displacements on a model of cracked material. We follow the numerical approach of Quintal et al. (2016, 2019), which couples the elasticity equations for the solid background (representing the rock grains) with the quasi-static, linearised Navier-Stokes equations for the laminar flow of a viscous fluid in the cracks. We neglect inertial terms, which is valid considering that wavelengths are much bigger than the size of analysed numerical models. Viscous friction between fluid particles inside the cracks due to FPD is the only possible cause for energy dissipation. Additionally, in Appendix A we calculate the reduced Reynolds number (Zimmerman & Main, 2004) and verify the validity of employing the linearised Navier-Stokes equations for the fluid flow inside the cracks induced by oscillatory displacements.

We solve the conservation of momentum equation, which, neglecting inertial terms, reduces to

$$\nabla \cdot \boldsymbol{\sigma} = 0, \tag{1}$$

where $\boldsymbol{\sigma}$ is the total stress tensor, considering a generalised constitutive equation, whose components in the frequency domain (Quintal et al., 2019) are

$$\sigma_{kl} = 2\mu\epsilon_{kl} + \lambda e\delta_{kl} + 2i\omega\eta\epsilon_{kl} - \frac{2}{3}i\omega\eta e\delta_{kl}, \tag{2}$$

where ϵ_{kl} are the components of the strain tensor, e is the cubical dilatation given by the trace of the strain tensor, δ_{kl} is the Kronecker delta, $\lambda = K - \frac{2}{3}\mu$ is the Lamé parameter written in terms of the bulk K and the shear μ moduli, η is the shear viscosity, ω is the angular frequency and i is the imaginary unit.

Eq. 2 is valid for the whole model since it is reduced to Hooke's law in the solid elastic background by setting the shear viscosity η to zero,

$$\sigma_{kl} = 2\mu\epsilon_{kl} + \lambda e\delta_{kl}, \tag{3}$$

and, inside the cracks Eq. 2 is reduced to

$$\sigma_{kl} = Ke\delta_{kl} + 2i\omega\eta\epsilon_{kl} - \frac{2}{3}i\omega\eta e\delta_{kl}, \tag{4}$$

because the shear modulus μ is zero in the fluid (e.g., Table 1). Combining Eqs. 1 and 4 yields the quasi-static, linearised Navier-Stokes equations, which describe a Newtonian flow inside the cracks.

2.2 Numerical upscaling

Our numerical models consist of two perpendicular cracks, that intersect each other at their centres, embedded in a solid elastic background representing the rock grains (Fig-

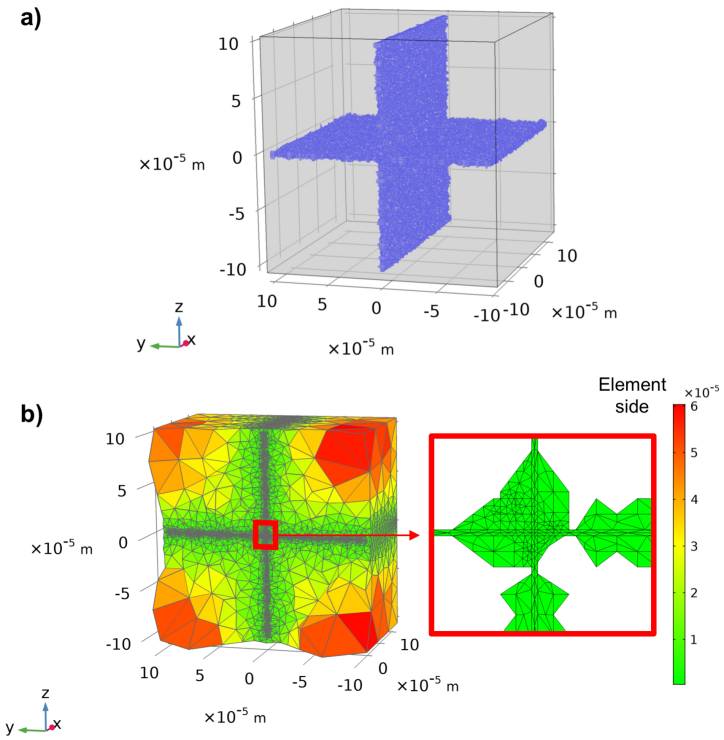

Figure 1. a) Numerical model consisting of two perpendicular and hydraulically interconnected cracks of $200\times200\times h$ μm^3 embedded in a cubic non-porous solid elastic background of $210\times210\times210$ μm^3. b) Mesh of the numerical model coloured according to the side length of each tetrahedral element. The inset of panel b shows the meshing inside the cracks only.

ure 1a). These models are a representative elementary volume (REV) of periodic media consisting of a repetition of these fundamental blocks (Appendix B). We consider cracks having a length of 200 μm and, depending on the model, the apertures (h) varying from 0.3 to 2.7 μm (in the case of planar cracks that would be equivalent to aspect ratios that vary from 0.0015 to 0.0135). The REV is a cube of 210 μm side. These models build up media having porosities from 0.2% to 2%. We have chosen the approximate crack dimensions based on the statistical analysis of thermally cracked rock samples described by Delle Piane et al. (2015). We employ material properties of quartz for the grains (Mavko et al., 2009) and of glycerin for the fluid filling the cracks (Table 1), as commonly used in forced-oscillations laboratory experiments so that the frequencies at which maximal squirt flow effects are expected fall within the seismic frequency range. In order to study the role played by the roughness of the cracks on the squirt flow mechanism, the aperture distribution of the cracks has been generated following the approach introduced by Nolte and Pyrak-Nolte (1991). The full workflow for the model generation is described by Lissa et al. (2019).

To calculate the P-wave modulus dispersion and attenuation, we solve equations 1 and 2 using a finite element direct solver from COMSOL Multiphysics. The numerical models are discretised in tetrahedral elements with side length represented by the colour bar in Figure 1b. The smallest elements are located inside the cracks, where energy dissipation occurs. The number of tetrahedral elements depends on the model. The number increases due to an increase in the wall roughness or due to a decrease in the aperture. This is because the mesh elements increase their size from the crack to the grains

and, consequently, a smaller aperture, as well as a rough wall, require smaller element sizes. In general, the total number of elements is around 1'000'000 for the cracks and 1'000'000 for the grains. We numerically perform quasi-static relaxation tests by applying an oscillatory displacement at the top boundary of the models. Additionally, normal solid displacements are set to zero on the lateral and bottom boundaries of the models. Assuming an incident wavelength much bigger than the REV size, the effective P-wave modulus (H) in the vertical direction (z) and corresponding attenuation (Q^{-1}) are obtained by volumetrically averaging the vertical component of the stress and strain fields in the entire spatial domain (O'Connell & Budiansky, 1978):

$$H(\omega) = \frac{\langle \sigma_{zz}(\omega) \rangle}{\langle \epsilon_{zz}(\omega) \rangle}, \tag{5}$$

$$Q^{-1}(\omega) = \frac{\langle Im[H(\omega)] \rangle}{\langle Re[H(\omega)] \rangle}, \tag{6}$$

where $\langle \sigma_{zz}(\omega) \rangle$ and $\langle \epsilon_{zz}(\omega) \rangle$ represent the volumetric averages of σ_{zz} and ϵ_{zz} for each frequency (Lakes, 2009; Jänicke et al., 2015) and Re and Im correspond to the real and imaginary parts of a complex number.

Given that the crack tips in our numerical models are close to the model boundaries, elastic interaction effects between the cracks are expected to occur, which are accounted for in our numerical approach (Guo et al., 2018). Nevertheless, in some cases, the stress and strain fields in the sample and those imposed at the boundaries may not be compatible with the assumed periodicity, which is manifested as disturbed fields at the boundaries. We performed a test for assessing possible undesired boundary effects (Milani et al., 2016). The test consists on comparing the effective P-wave modulus response of our model, or the repeating unity cell, with that of a model formed by an assembly of 4 identical repeating unity cells. The results, which are reported in Appendix B, show that there are no boundary artefacts affecting the numerical results.

2.3 Local energy dissipation

For a better understanding on how the energy dissipation occurs in the interconnected cracks, we calculated the local contribution $1/q_n$ to the total attenuation $1/Q$ from each element Ω_n of our 3D model as function of frequency as follows (Solazzi et al., 2016; O'Connell & Budiansky, 1978):

$$\frac{1}{q_n(\omega)} = \frac{\langle \Delta P_n(\omega) \rangle / \delta_n^3}{2\omega \langle W(\omega) \rangle}, \tag{7}$$

where $\langle \Delta P_n(\omega) \rangle$ and $\langle W(\omega) \rangle$ are the average power dissipated per cycle in harmonic loading from each considered element of volume δ_n^3 and the average strain energy per cycle in the whole domain, respectively, given by Quintal et al. (2019)

$$\begin{aligned} \langle \Delta P_n(\omega) \rangle = 2\eta Re[&\dot{\epsilon_{xx}}\dot{\epsilon_{xx}}^* + \dot{\epsilon_{yy}}\dot{\epsilon_{yy}}^* + \dot{\epsilon_{zz}}\dot{\epsilon_{zz}}^* + \dot{\epsilon_{xy}}\dot{\epsilon_{xy}}^* + \dot{\epsilon_{xz}}\dot{\epsilon_{xz}}^* + \dot{\epsilon_{yz}}\dot{\epsilon_{yz}}^* \\ &- \frac{1}{3}\left(\dot{\epsilon_{xx}} + \dot{\epsilon_{yy}} + \dot{\epsilon_{zz}}\right)\left(\dot{\epsilon_{xx}} + \dot{\epsilon_{yy}} + \dot{\epsilon_{zz}}\right)^*]_n \delta_n^3, \end{aligned} \tag{8}$$

and

$$\langle W(\omega) \rangle = \sum_{\Omega} \frac{1}{4} Re\left[\dot{\sigma_{xx}}\dot{\epsilon_{xx}}^* + \dot{\sigma_{yy}}\dot{\epsilon_{yy}}^* + \dot{\sigma_{zz}}\dot{\epsilon_{zz}}^* + \dot{\sigma_{xy}}\dot{\epsilon_{xy}}^* + \dot{\sigma_{xz}}\dot{\epsilon_{xz}}^* + \dot{\sigma_{yz}}\dot{\epsilon_{yz}}^*\right]_n \delta_n^3, \tag{9}$$

where a dot on top of a variable implies the multiplication of the variable by $i\omega$ and the symbol $*$ denotes the complex conjugate of the variable. The total attenuation can be obtained as the sum in the whole model of the local contribution $1/q_n$ weighted by each element volume, that is,

$$\frac{1}{Q(\omega)} = \sum_{\Omega} \frac{1}{q_n(\omega)} \delta_n^3. \tag{10}$$

3 Results

We estimate the effective P-wave modulus dispersion and attenuation caused by squirt-flow between hydraulically interconnected cracks by numerically applying quasi-static, oscillatory relaxation tests to models such as the one shown in Figure 1a. The squirt flow process is usually described as the compression of a compliant pore or crack which is connected to a stiffer one. In our models we consider vertical oscillatory compression emulating the deformation caused by a P-wave with vertical (z) incidence and a wavelength much bigger than the model. Consequently, the horizontal crack behaves as the compliant pore while the vertical one, which remains nearly undeformed, behaves as the stiff pore. We first consider a simple crack walls roughness which corresponds to a binary distribution of apertures in the cracks and, then, we extend the analysis to more complex roughness of the crack walls by considering fully variable apertures. In both cases, the cracks are completely open (i.e., no contact areas). We also compute the hydraulic apertures of the crack models according to the workflow described in Appendix C. The P-wave modulus and attenuation for planar cracks having such hydraulic apertures are compared with that of the binary and fully variable aperture crack models to help understanding the effects of rough crack walls. Finally, we emulate an increase in the confining pressure on certain models by applying a uniform reduction of the crack apertures which, in turn, creates contact areas.

3.1 Cracks with binary aperture distribution

First, we consider aperture distributions with only two possible aperture values. Figure 2 shows a model of interconnected cracks having a minimum aperture, a maximum aperture and no intermediate ones, here referred to as a binary model. The cracks are embedded in a non-porous elastic solid cube as shown in Figure 1a. We consider six different binary aperture distributions, which are illustrated in Figure 3. Additionally, the cracks are symmetrical with respect to their central plane. In those models, the percentages of the crack having the minimum aperture of 0.3 μm are 2.5%, 5%, 7.5%, 10%, 20% and 50%, while the rest of the crack has the maximum aperture of 2.7 μm. This means that cracks with 100% and 0% of minimum aperture h_{min} are planar cracks (i.e., have constant aperture) with apertures of 0.3 μm and 2.7 μm, respectively.

The P-wave modulus and corresponding attenuation in the vertical direction for the binary models, with aperture distributions shown in Figure 3, are plotted in Figure 4. The compression of the horizontal crack, due to the vertical deformation, generates a fluid pressure gradient between the highly compressed horizontal crack and the nearly undeformed vertical one. As a consequence, FPD occurs and energy is dissipated due to friction between layers of the viscous fluid. For validation of our numerical simulations, we obtained the low- (LF) and high-frequency (HF) limits following the approaches of Gassmann (1951) and Mavko and Jizba (1991), respectively. In the first case, we numerically compute the anisotropic dry stiffness matrix from 6 relaxation test by extending the 2-D methodology of Rubino et al. (2016) to 3-D for the planar crack model having 2.7 μm of aperture and under dry conditions. Then, using Gassmann's equations, we calculate the saturated stiffness matrix (P-wave modulus with vertical incidence obtained from this analysis is shown as dotted black line). At the LF limit, the P-wave modulus depends on the porosity of the rock and, thus, it changes with the percentage of h_{min}. For the HF limit, we consider no hydraulic communication between cracks. For that, we employ a boundary condition within the cracks that restricts the fluid flow to zero between cracks. The numerically obtained P-wave modulus in the vertical direction for the saturated planar crack model having 0.3 μm of aperture is shown as red dotted line. The increase in the percentage of h_{min} in the crack aperture distributions, increases the P-wave modulus at the LF and HF limits, stiffening the models due to the reduction in the crack volume.

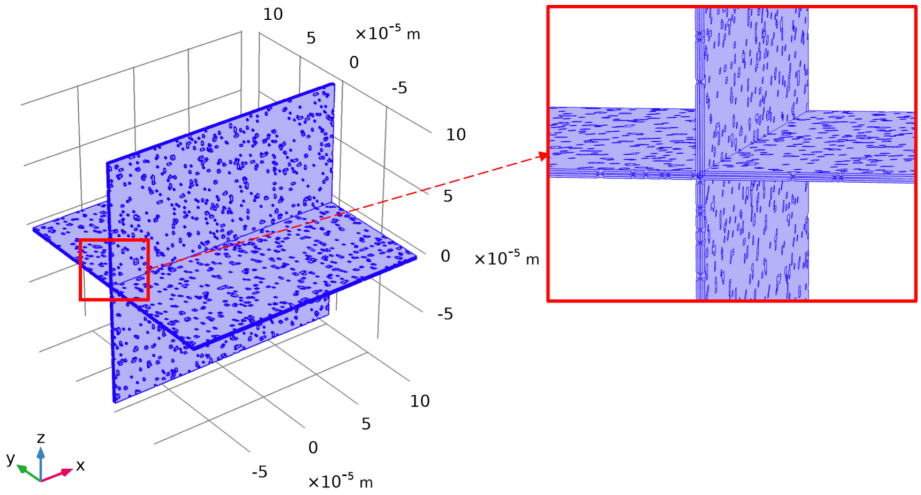

Figure 2. Example of one model having two hydraulically interconnected cracks with a binary aperture distribution, i.e., only two apertures of $h_{min} = 0.3$ μm (5% of crack area) and of $h_{max} = 2.7$ μm (95% of crack area) are present. The distribution of the minimum aperture zones is uncorrelated.

Considering now the attenuation responses, we observe in Figure 4 (bottom) that the binary models having 5% to 20% of h_{min} exhibit two attenuation peaks at characteristic frequencies fc_1 close to 10 Hz and fc_2 close to 10^4 Hz. Based on theoretical solutions for the squirt flow characteristic frequency of the form $f_c \sim \frac{K}{\eta} (\frac{h}{L})^3$ (e.g., Gurevich et al., 2010), the two attenuation peaks suggests that there are two characteristic aspect ratios or apertures playing a role in the energy dissipation. The characteristic frequency fc_2 is located near to that observed for 0% of h_{min} (i.e., h=2.7 μm), while fc_1 is closer to the characteristic frequency observed for 100% of h_{min}. The magnitude of the high-frequency attenuation peak decreases and the one of the low-frequency peak increases as the percentage of h_{min} in the crack aperture increases. Moreover, the transition between dominating peaks occurs for a percentage of h_{min} as low as 10%.

To gain a better understanding of where the energy dissipation occurs we apply the methodology described in Section 2.3. Figure 5 shows the local contribution $1/q_n$ (Eq. 7) to the total attenuation $1/Qp$ in horizontal slices within the horizontal crack for the model having 5% of the h_{min} at the frequencies fc_1=10 Hz and fc_2=10^4 Hz. The colour-bar range is fixed equally for both considered frequencies in order to clearly represent the magnitude differences. The colour plots correspond to two horizontal slices (xy-planes) at z=0 μm (top) and z=1.05 μm (middle). Despite the fact that $1/q_n$ is maximal in the cracks intersection for both frequencies, they present a minor contribution to the overall dissipation. At the bottom, the sum of the $1/q_n$ over each horizontal slice within the crack is plotted for both frequencies. In agreement with the attenuation curve in Figure 4 (blue solid line), the local contribution $1/q_n$ corresponding to fc_2 presents the highest magnitudes. Important differences regarding where energy is being dissipated can be observed for the two frequencies. Although energy dissipation is reasonably similar in the middle plane (z=0 μm) for both frequencies, there is a significant difference between them in the plane outside the aperture h_{min}, closer to the walls of the cracks (z=1.05 μm). Furthermore, dissipation is much more concentrated within $abs(z) < h_{min}$ at fc_1 than at fc_2. From the sum of $1/q_n$ over each horizontal slice within the cracks (bottom), we observe for fc_1 high concentration of energy dissipation within the minimum aperture (h_{min}) for the whole horizontal crack. Consequently, for the binary mod-

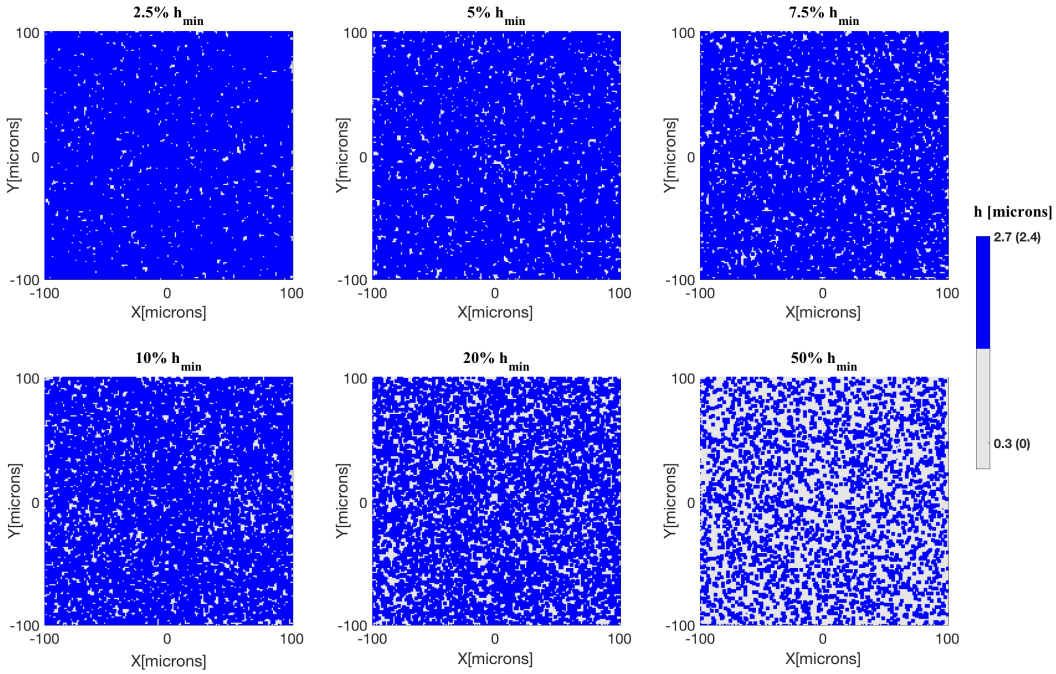

Figure 3. Aperture distributions employed in the model of Figure 2 containing two identical and perpendicular cracks with binary apertures: $h_{min} = 0.3$ μm (varying from 2.5% to 50% of crack areas) and $h_{max} = 2.7$ μm (for the remaining percentage of crack wall areas). In addition, the apertures between parenthesis correspond to the crack conditions after an increase of the confining pressure described in Section 3.3.

els (Figure 4) the attenuation at fc_1 is controlled by the minimum aperture while at fc_2 the attenuation is controlled by a bigger aperture.

To better illustrate where energy dissipation occurs at each frequency within a crack for the model having 5% of the h_{min}, we calculate the sum of the local contribution to the attenuation in the horizontal crack as a function of z (vertical coordinate) at six frequencies (Figure 6, top). The area under each curve after multiplying each $1/q_n$ by their element volume (i.e., δ_n^3) represents the contribution of the energy dissipation inside the horizontal crack to the total attenuation for the considered frequencies. Energy dissipation outside the minimum aperture, increases from low- to high-frequency until reaching its maximum at $fc_2 = 10^4$ Hz. Although energy dissipation for $f = 10$ Hz is lowest outside h_{min}, inside the minimum aperture it reaches higher magnitudes similar to the other considered frequencies. Figure 6 (bottom) shows the contribution to the total attenuation ($1/Qp$) taking place inside the minimum aperture (blue circles) as well as the total attenuation (green solid line) for the model having 5% of h_{min}. The excellent match between the curves at the low frequency peak confirms that the minimum aperture (h_{min}) has predominant control over attenuation at fc_1.

3.1.1 Effect of hydraulic apertures

Relating the hydraulic behaviour of a cracked-model with its P-wave modulus dispersion and attenuation requires quantifying the hydraulic transmissivity of the crack which is controlled by its aperture distribution. Even though the hydraulic transmissivity of the media considered in this work is zero, since the cracks are not in contact with

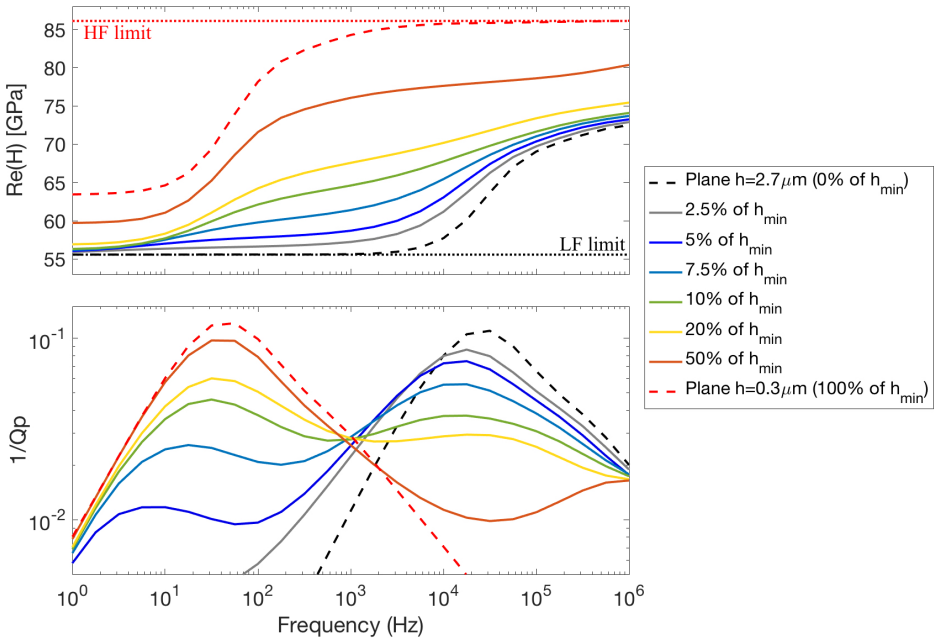

Figure 4. Real part of the P-wave modulus Re(H) and attenuation 1/Qp as functions of frequency for the interconnected cracks presented in Figure 3 and for pairs of interconnected planar cracks with aperture of 0.3 or 2.7 μm. In addition, P-wave modulus at low- and high-frequency limits following Gassmann (1951) and Mavko and Jizba (1991) approaches, respectively, are shown in dotted lines for the planar crack models having 0.3 μm (red dotted lines) and 2.7 μm (black dotted lines) of aperture.

the REV boundaries, the local transmissivity within each crack governs squirt flow between the connected cracks. We then focus on the fluid flow behaviour of each crack (the horizontal and vertical cracks are equal in our models). We use the numerical methodology described in Appendix C to obtain the hydraulic apertures for some of the binary models shown in Figure 3.

Figure 7 (top) shows the calculated arithmetic and harmonic mean of apertures, and hydraulic apertures for the binary models having from 5% to 70% of h_{min} in their aperture distributions. In agreement with Beran (1968); Silliman (1989); Zimmerman and Main (2004), our results for the hydraulic aperture are bounded by the arithmetic $\langle h^3 \rangle$ and harmonic $\langle h^{-3} \rangle^{-1}$ means. Most importantly, the hydraulic aperture takes values similar to the harmonic mean and much closer to h_{min} even though h_{min} represents less than 50% of the crack. Figure 7 (bottom) shows the total attenuation magnitudes for the binary models at the two discussed characteristic frequencies, as function of h_{min} percentage. The attenuation at fc_1 is higher than at fc_2 already from 10% of h_{min} and from 50% it is close to the maximum value possible (that for the plane crack with 100% of h_{min}, Figure 4). Thus, for these models, both the hydraulic aperture and the characteristic frequency of the maximum attenuation are predominantly governed by the minimum aperture once it exceeds 50%.

Figure 8 shows the P-wave modulus dispersion and attenuation of the three binary models having 5%, 10% and 50% of h_{min}, together with that of three models having cracks with a constant aperture equal to the corresponding hydraulic apertures. The match between the dominating characteristic frequency (fc_2) of the binary model with 5% of h_{min} (blue curves) and that one of a model with planar cracks whose aperture is equal to the

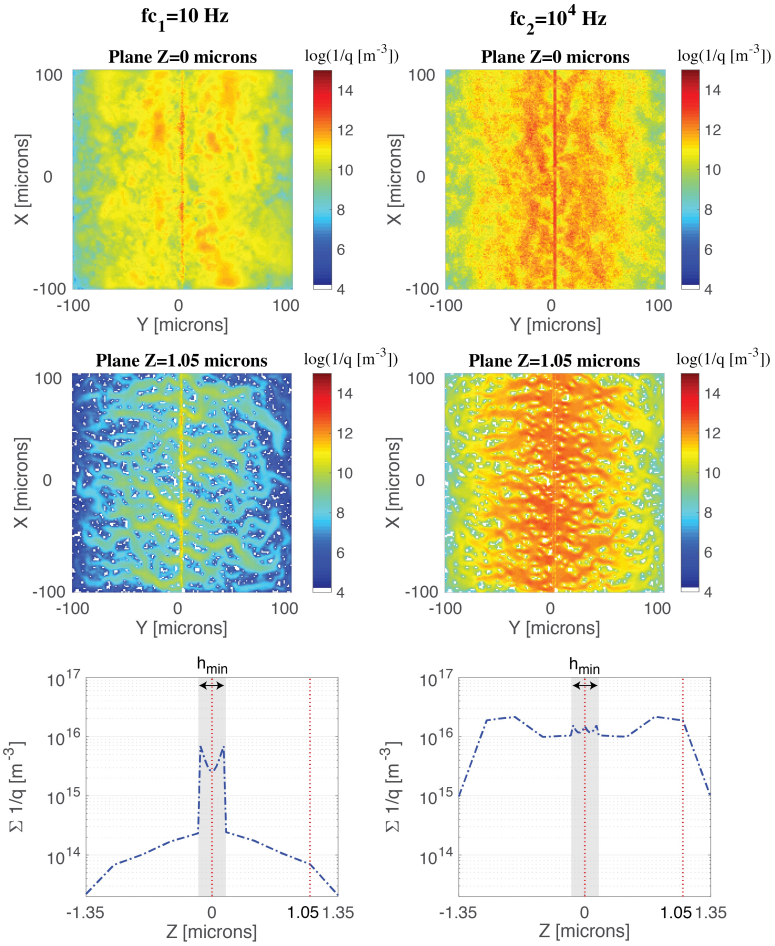

Figure 5. Local contribution $1/q_n$ (Eq. 7) to the total attenuation $1/Q$ at $fc_1 = 10$ Hz (left) and $fc_2 = 10^4$ Hz (right) in two horizontal slices (xy-planes), at z=0 μm (top) and z=1.05 μm (middle), for the binary model of Figure 3 having 5% of h_{min}. At the bottom, the sum of the $1/q_n$ for each horizontal slice within the crack is plotted for both frequencies.

hydraulic aperture indicates that the latter controls the main attenuation peak caused by squirt-flow in this model. When there is not a clear dominating attenuation peak, such as, for 10% of h_{min} (green curves), the fc of the planar model having the hydraulic aperture is still located close to fc_2. The fc of the binary model having 50% of h_{min}, on the other hand, matches the fc_1 corresponding to an aperture of 100% of h_{min} or $h = 0.3$ μm (shown in Figure 4). Meanwhile, the planar model having the hydraulic aperture of the model with 50% of h_{min} predicts a characteristic frequency located one order of magnitude higher than that of the corresponding binary model. Which emphasis that it is the h_{min}, and not the hydraulic aperture, the one controlling the energy dissipation process for this model.

3.2 Cracks with more intricate rough walls

The analysis presented in Section 3.1 deals with simple models to understand the effects that cracks with rough walls have on squirt flow. However, their abrupt changes

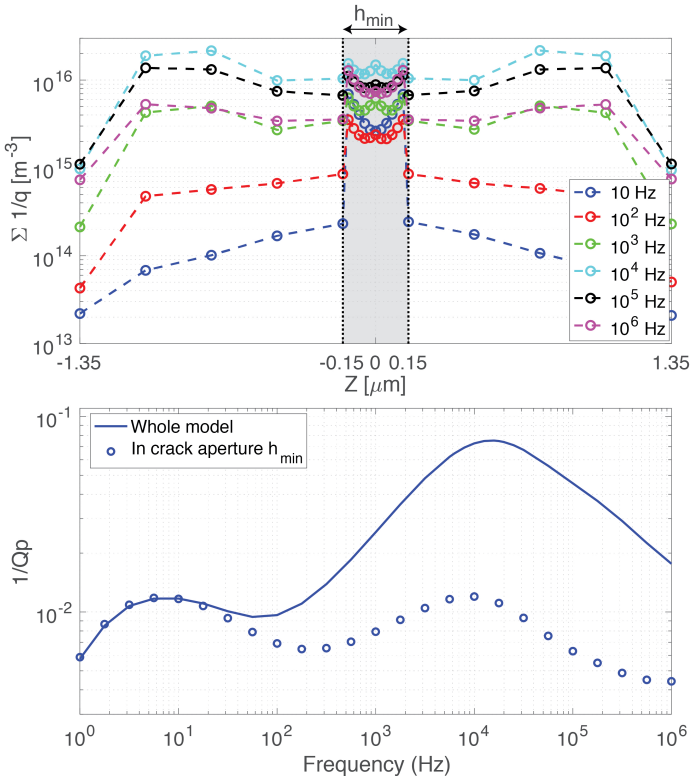

Figure 6. Sum of the local attenuation contribution $1/q_n$ for each horizontal slice within the horizontal crack at six frequencies (top) and the total attenuation (blue solid line) with the volumetric integration of $1/q_n$ only inside aperture h_{min} (blue circles) as a function of frequency (bottom) for the binary model having 5% of h_{min}.

in aperture are expected to unrealistically enhance the influence of the aperture variation. In this section we consider more realistic aperture distributions (Figure 9), but still considering symmetric rough walls. The two numerical models A and B have cracks with fully variable apertures, with 20% of $h_{min} = 0.3$ μm and equal arithmetic mean aperture $h_{mean} = 2.7$ μm. Model A presents a regular distribution of zones having apertures equal to h_{min} (white zones), which we refer to as uncorrelated distribution, while Model B has the zones with h_{min} gathered in broader areas, i.e., correlated distribution. To quantify the amount of variation of their apertures, we compute the standard deviation (std). Model B has a higher standard deviation (std_B=2.55 μm) than Model A (std_A=1.9 μm). Figure 10 (top) shows the real part of the P-wave modulus and attenuation for both models. For comparison, the same curves of planar crack models having crack apertures equal to h_{min} and h_{mean} are also included. The P-wave modulus at the LF and HF limits of both models tend to converge to that of the planar crack model having the same mean aperture h_{mean} (black dashed curve). Due to the absence of contact ares, the crack density (given by the number of cracks and their surface in a certain volume) controls the stiffness of the models (Kachanov & Mishakin, 2019). The crack density is high and equal in all our models, which means that the difference is their stiffness is controlled by the difference in the crack volumes of the models. Moreover, provided that all models have the same area in the xy-plane (200×200 μm^2), the arithmetic mean of the apertures is the only geometrical parameter controlling the crack volumes. Therefore, we refer to the aperture controlling the elastic response of the fracture (h_{mean}) as the mechanical aperture. Interestingly, Model A has a clearly defined dominating attenuation peak

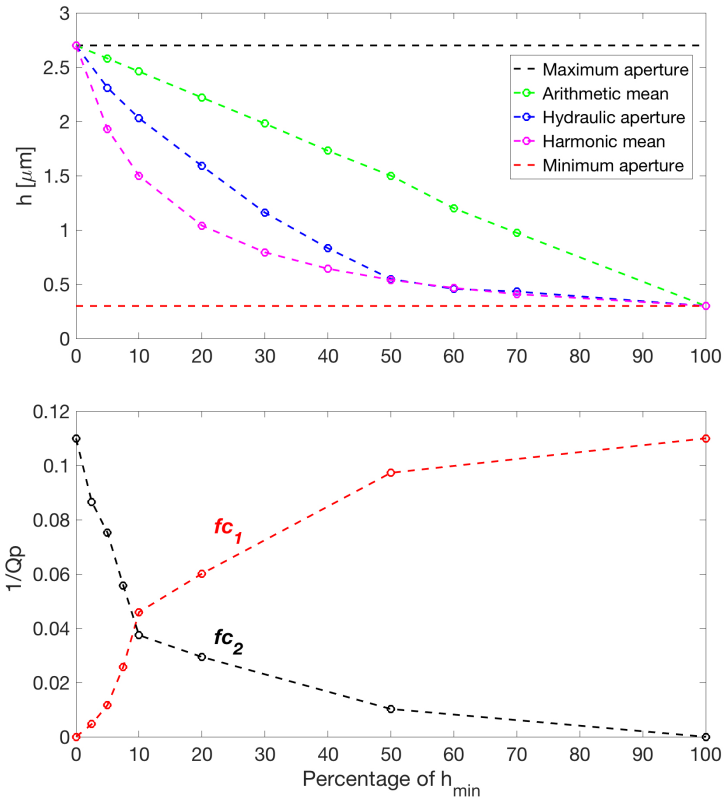

Figure 7. Arithmetic mean, harmonic mean and hydraulic apertures for binary model having from 5% to 70% of h_{min} in their apertures. Also h_{min}=0.3 μm and h_{max}=2.7 μm are plotted in dashed lines for reference (top). Seismic attenuation ($1/Qp$) for the binary models of Figure 3 at the characteristic frequencies as functions of h_{min} (bottom).

Table 2. Apertures for crack models presented in Figure 9

Model	Minimum	Arithmetic mean	Hydraulic
A	$h_{min} = 0.3$ μm	$h_{mean} = 2.7$ μm	$h_H = 1.31$ μm
B	$h_{min} = 0.3$ μm	$h_{mean} = 2.7$ μm	$h_{Hx} = 1.28$ μm ; $h_{Hy} = 1.92$ μm

in the considered frequency range while Model B presents a broader attenuation curve. This is explained by the fact that Model B has a higher standard deviation of the crack aperture than Model A, which implies that more crack apertures are playing a role in the attenuation response. Figure 10 also shows the P-wave modulus dispersion and attenuation of planar crack models having the hydraulic apertures of Model A and B (2). The characteristic frequency of the planar crack model with aperture h_H in y-direction, which is the same as the fluid flow in the oscillatory test for Model B, matches the frequency range corresponding to the maximum attenuation for Model B. On the other hand, the characteristic frequency of Model A, which is dominated by h_{min}, is significantly lower than the one associated with the planar crack model with aperture h_H. This means that the distribution of zones having apertures equal to h_{min} (i.e., correlated or uncorrelated) also plays a role in the characteristic frequency.

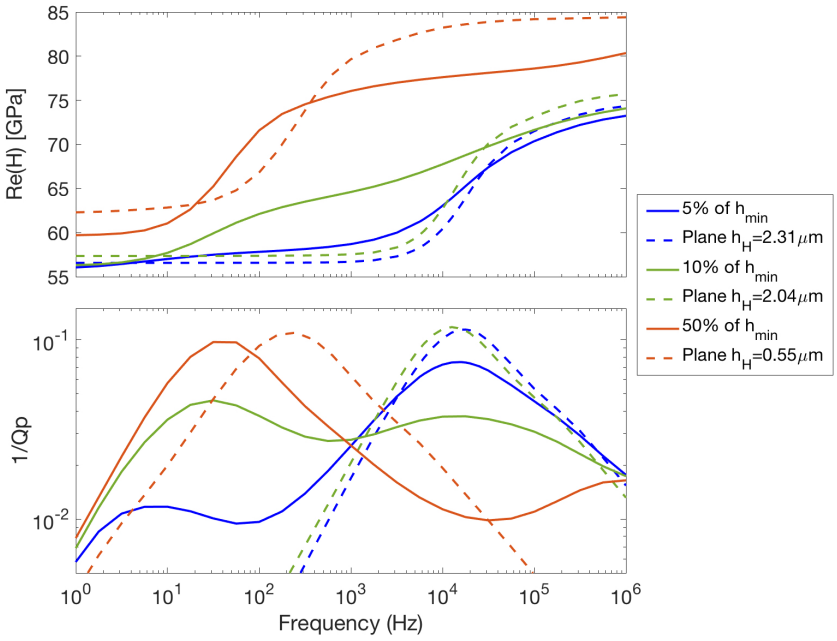

Figure 8. Real part of the P-wave modulus and attenuation for binary models having 5%, 10% and 50% of h_{min} (solid lines) and the ones corresponding to planar crack models having their equivalent hydraulic apertures, that is h_H=2.31 μm, h_H=2.04 μm and h_H=0.55 μm, respectively (dashed lines).

3.3 Cracks with contact areas

Laboratory measurements of seismic attenuation on fluid-saturated rock samples are usually obtained under variable confining pressure at ranges affecting the rocks in subsurface (e.g., Subramaniyan et al., 2015; Pimienta et al., 2015; S. Chapman et al., 2019). The increase of confining pressure on cracked rock samples produces the occurrence of contact areas between crack walls or compliant pores, which in turns increases the overall stiffness of the rock (Shapiro, 2003). For analysing the corresponding effects on squirt-flow, we emulate an increase in confining pressure by introducing an uniform reduction in the crack apertures.

We first consider the binary uncorrelated crack models of Figure 3 having 5% and 10% of h_{min}=0.3 μm and we apply a uniform reduction of 0.3 μm. This yields a reduction of the maximum aperture from 2.7 to 2.4 μm and the occurrence of 5% and 10% of contact area density (CAD), respectively (apertures in brackets in the colour bar of Figure 3). We numerically estimate the hydraulic apertures of those models following the methodology outlined in Appendix C (Table 3). Figure 11 shows the P-wave modulus dispersion and attenuation for the considered models with and without contact areas, emulating their opening state before and after an increase in the confining pressure, as well as the response of planar crack models having the hydraulic aperture of the models with contact areas. The increase in the confining pressure produces a stiffening of the cracks, as seen from the overall reduction of P-wave modulus dispersion and attenuation. As expected, such effects are larger for the model with 10% of CAD due to the further reduction in pore space. In addition, the low-frequency attenuation peak vanishes due to the closure of the minimum aperture. The characteristic frequencies of the planar crack models with the corresponding hydraulic apertures are in qualitative agreement with that of the models with contact areas. Nevertheless, significant discrepancies between their

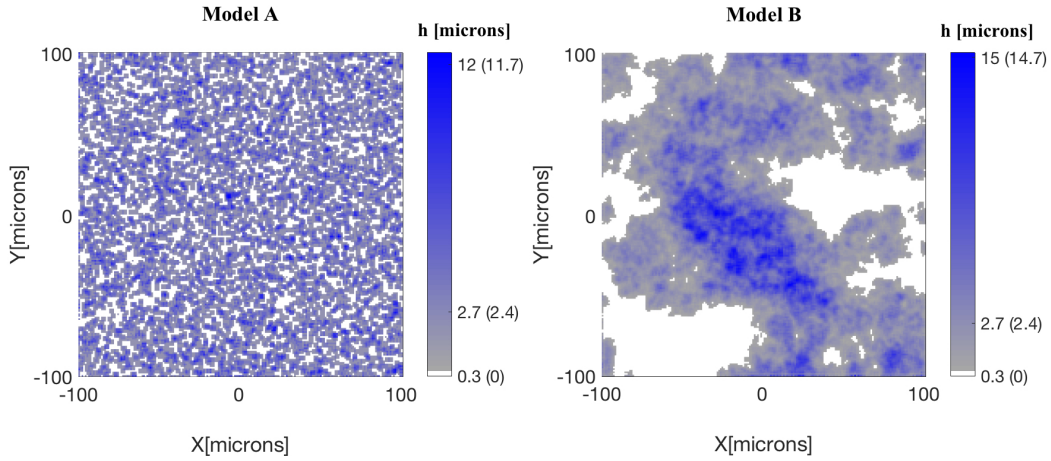

Figure 9. Aperture of cracks having rough walls with uncorrelated (Model A) and correlated (Model B) distributions of zones of minimum aperture $h_{min} = 0.3$ μm (white zones). In addition, the apertures between parenthesis correspond to the crack conditions after an uniform reduction in the apertures that emulates an increase of the confining pressure.

Table 3. Apertures for crack binary models with contact areas

Model	Minimum	Maximum	Arithmetic Mean	Hydraulic
5% CAD	$h_{min} = 0$ μm	$h_{max} = 2.4$ μm	$h_{mean} = 2.28$ μm	$h_H = 2.12$ μm
10% CAD	$h_{min} = 0$ μm	$h_{max} = 2.4$ μm	$h_{mean} = 2.16$ μm	$h_H = 1.85$ μm

attenuation magnitude can be observed, which emphasises the necessity of employing three apertures to describe the squirt flow process: the mechanical aperture governing the P-wave magnitude at the frequency limits (we showed that it is the mean aperture in absence of contact areas), and the minimum and hydraulic apertures having control on the characteristic frequencies of the attenuation curve. In presence of contact areas (i.e., h_{min}=0 μm), only the mechanical and hydraulic apertures control the squirt flow effects.

We extended the analysis of contact area effects to the models with fully variable apertures presented in Figure 9. A uniform reduction in their apertures of 0.3 μm closes the cracks in the areas with previous apertures of h_{min} and equally reduces the rest of their aperture. Therefore, both models have 20% of contact area density after an increase in the confining pressures. Table 4 shows their relevant apertures and Figure 12 presents their P-wave modulus dispersion and attenuation. The responses from planar crack models having their hydraulic aperture as well as models from Figure 9 without contact areas are also included in the analysis. From the analysis of Figure 10, we know that the attenuation of Model A occurs mostly at low-frequencies, being governed by the minimum aperture. Given that the increase in the confining pressure closes the minimum aperture, Figure 12 shows that Model A with contact areas presents negligible P-wave modulus dispersion and attenuation. For the same reason, the emulated increase in the confining pressure in Model B concentrates most of the remaining attenuation at high-frequencies. Comparison between Model B with contact areas and that of the planar cracks having its hydraulic aperture h_H present relatively large discrepancies on their attenuation and P-wave modulus magnitudes.

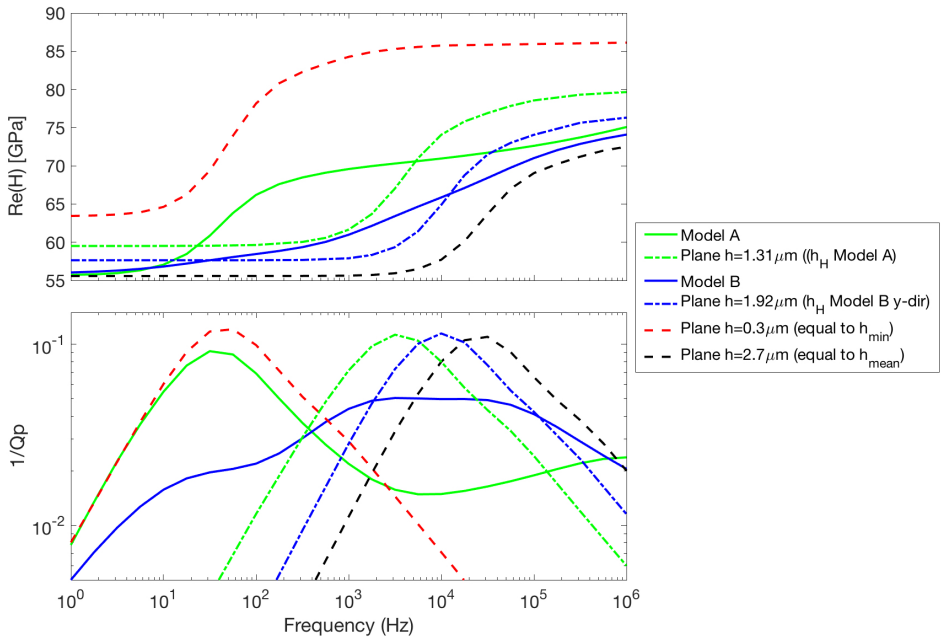

Figure 10. Real part of the P-wave modulus and attenuation as functions of frequency for the interconnected cracks presented in Figure 9 and for interconnected planar cracks having the minimum, the mechanical and the hydraulic apertures of the Models A and B.

Table 4. Apertures for crack models with contact areas presented in Figure 9

Model	Minimum	Arithmetic Mean	Hydraulic
A with CA	$h_{min} = 0$ μm	$h_{mean} = 2.4$ μm	$h_H = 1.11$ μm
B with CA	$h_{min} = 0$ μm	$h_{mean} = 2.4$ μm	$h_{Hy} = 1.5$ μm

4 Discussion

The aim of the present contribution was to analyse the effects that the roughness of the crack walls has on the P-wave modulus dispersion and attenuation caused by squirt flow and to investigate whether there are certain crack apertures that could be used to interpret this physical process. The considered numerical models are in the micro-scale, or pore scale. We followed the proposed hydromechanical approach of Quintal et al. (2016, 2019) coupling the equations of an elastic background, and fluid filled cracks described by the quasi-static, linearised Navier-Stokes (LNS) equations. Quintal et al. (2016) showed an equivalency between the results based on the LNS and poroelastic Biot's equations at the mesoscale. Therefore, it is expected that similar results as those observed for micro cracks in this study hold for mesoscale fractures exhibiting rough walls.

The roughness in the crack walls considered in our first models was not allowed to produce contact areas. Such constrain implies that the volume of the cracks controls the P-wave modulus values at the LF and HF limits. Therefore, the P-wave modulus of the models with rough cracks (Models A and B) converge to those of a model with planar cracks having their mean aperture at the LF and HF limits. This means that the mechanical aperture is represented by the arithmetic mean aperture without influence of the wall roughness. The inclusion of contact areas increases the model stiffness and, then, contact areas density and distribution start playing a role on the effective response of

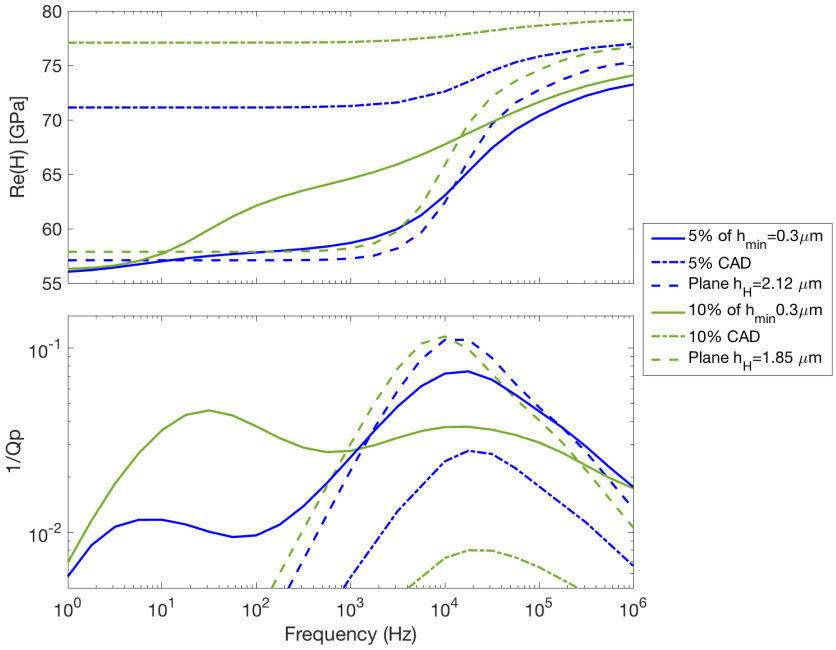

Figure 11. Real part of the P-wave modulus and attenuation as functions of frequency for the interconnected cracks presented in Figure 3 having 5% and 10% of contact area density (CAD) and for interconnected planar cracks having their equivalent hydraulic apertures. Same curves of those models with binary aperture before the emulated confining pressure increment are also included.

the models (e.g., Hudson & Liu, 1999). By analysing the attenuation curves, we observed that the occurrence of contact areas significantly reduces the attenuation magnitude and that their stiffening effects are higher for Model A, which has an uncorrelated aperture distribution, than for Model B which has a correlated one. For Model B, the aperture reduction giving rise to contact areas resulted in significant changes in the P-wave modulus dispersion and attenuation. On the other hand, since the attenuation for Model A was dominated by the minimum aperture, the aperture reduction caused the magnitude of attenuation to be reduced to negligible levels.

Our results show that rock image simplifications or errors commonly associated with DRP methods can significantly affect the calculations of the P-wave modulus dispersion and attenuation as well as the hydraulic transmissivity of cracks. For the analysed binary models, for example, we observed that a minor change in the percentage of h_{min} (from 5% to 20%) can shift the attenuation peak from 10^4 Hz to 10 Hz. In addition, we show that the characteristic frequency is not controlled by the arithmetic mean aperture of the cracks having rough walls. This relevant observation must be considered when crack apertures are estimated from the characteristic frequency, for example, in laboratory experiments. Effects of roughness of crack walls, as well as the contact area distribution, need to be accounted for when comparing certain experimental measurements with DRP estimations.

In analytical solutions for computing seismic attenuation and moduli dispersion due to squirt-flow, the characteristic frequency corresponding to the attenuation peak is related to the cubic of an aperture h (among other parameters), which is the aperture of a crack with smooth parallel walls (e.g., Gurevich et al., 2010). Based on those analytical solutions, the characteristic frequencies of all the planar crack models considered in

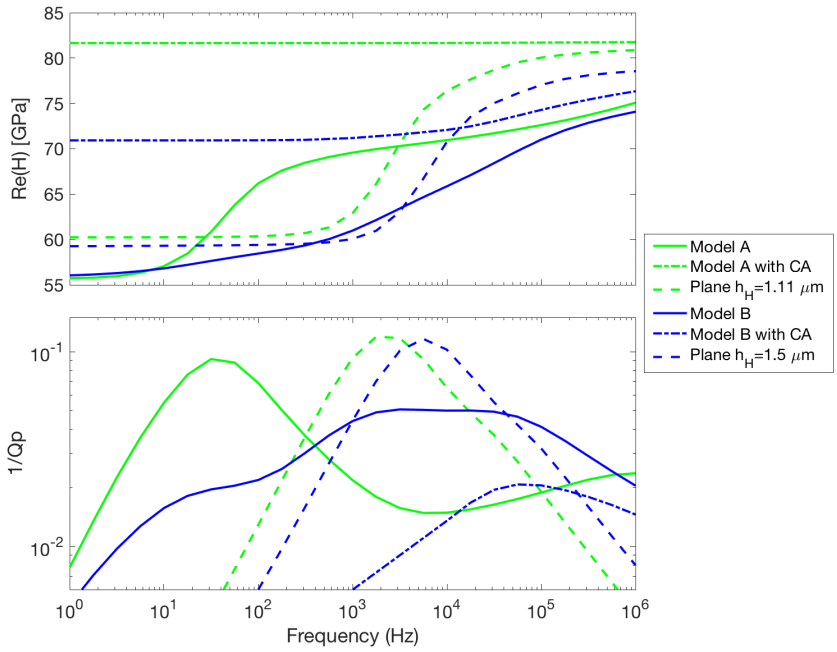

Figure 12. Real part of the P-wave modulus and attenuation as functions of frequency for the interconnected cracks presented in Figure 9 having 20% of contact areas and for interconnected plane cracks having their hydraulic apertures. Same curves of Models A and B before the emulated confining pressure increment are also included.

this work can be approximated as $f_c \sim \frac{1}{2}\,\frac{K_S}{\eta}\,(\frac{h}{L})^3$, where K_S is the bulk modulus of the solid (i.e., rock grains), η the fluid viscosity, h the aperture of the cracks and L is the diameter of a penny-shape crack having the same surface as our rectangular cracks (i.e., L=226 μm). Our work showed that the characteristic frequency of cracks with rough walls is mostly related to the minimum aperture h_{min} and/or the hydraulic aperture h_H depending on the percentage of h_{min} present in the crack and on the presence of contact areas. Moreover, we showed that each aperture present in the crack aperture distribution makes a contribution to the attenuation curve. In other words, there is a different aperture dominating the attenuation at each frequency. Therefore, assuming a link between aperture and the fluid flow at a given frequency, a frequency-dependent hydraulic aperture could be considered for squirt flow. At the mesoscale, a frequency-dependent hydraulic conductivity for transient (oscillatory) flow is not a new concept (e.g., Dagan, 1982; Sanchez-Vila et al., 2006; Caspari et al., 2013). However, the numerically estimated hydraulic apertures of our work consider a stationary fluid flow inside the rough cracks. Since the P-wave modulus dispersion and attenuation respond to a frequency dependent phenomenon, the comparison between both approaches might not be completely fair. Nevertheless, our work highlights the importance of analysing the relation between the frequency dependent attenuation caused by squirt flow and the hydraulic aperture of the cracks.

5 Conclusions

We studied the effects that roughness in the crack walls have on squirt-flow by numerically simulating oscillatory relaxation tests on models containing interconnected cracks. Their effects were analysed in terms of the effective P-wave modulus dispersion and attenuation. We first considered models having cracks with wall roughness described as

binary aperture distributions, which allowed for the occurrence of only two apertures: h_{min} and h_{max}. In a step towards more complex models, we analysed the effects of two models with fully variable aperture of the cracks between h_{min} and h_{max} having correlated and uncorrelated distributions of h_{min} zones. At last, we emulated an increase in the confining pressure on those models by reducing the crack apertures, which allowed for the occurrence of contact areas. Additionally, we interpreted our results using a numerically estimated hydraulic aperture h_H of the considered rough cracks.

We observed that in absence of contact areas the arithmetic mean aperture of the cracks controls the stiffness of the models (P-wave modulus) at the high- and low-frequency limits. In addition, visualising the local contribution to the total attenuation curve, we observed that at each frequency a different aperture controls the energy dissipation process caused by squirt flow. This means that the higher the standard deviation of the aperture distribution is, the broader the attenuation curve will be. Moreover, we identified two main apertures controlling the peak frequencies of the attenuation curve. Predominantly, the minimum aperture h_{min} tends to govern the energy dissipation process, but in presence of contact areas or with significantly small percentage of h_{min}, the hydraulic aperture h_H might control the characteristic frequency.

Appendix A Reduced Reynolds number

We calculated the reduced Reynolds number (Zimmerman & Main, 2004)

$$Re^* = \frac{\rho U h}{\eta \Lambda}, \tag{A1}$$

that is the product of the traditional Reynolds number and the geometric parameter $\frac{h}{\Lambda}$, where ρ and η are the bulk density and viscosity of the fluid, U is the average velocity in the main flow direction, h is the mean crack aperture and Λ is the mean distance between asperities of the walls of the cracks.

According with Zimmerman and Main (2004), the condition for the inertia forces to be negligible compared with the viscous forces is that $Re^* \ll 1$. An upper limit for Re^* for the cases considered in our study corresponds to the binary model having 50% of h_{min} as it is the one having the minimum Λ=0.01 μm. As U increases with the frequency, we compute Re^* for the maximum considered frequency (i.e., 10^6 Hz of the oscillatory displacement). For the described case and a strain on the model of 10^{-5} (similar to the ones impose in laboratory experiments), we obtained $U \approx 5 \times 10^{-5}$ and $Re^* \approx 1 \times 10^{-5}$, which comfortably satisfy the condition for the inertia forces to be negligible compared with the viscous forces.

Appendix B REV boundary effects

Given the dimensions of the numerical model used for our analysis, we followed the methodology employed by Milani et al. (2016) to verify the absence of boundary effects affecting the results. For that, we consider our REV (Figure 1) to be a repeating unit cell (RUC) and created a model consisting of four RUCs as shown in Figure B1. Following the methodology presented in Section 2 we calculate the P-wave modulus and the attenuation for models consisting of one and four RUCs having planar crack with an aperture of 2.7 μm. The choice of such an aperture is based on the fact that this model is the most compliant from all the considered models in this work and, consequently, the most likely to present boundary effects as shown by Milani et al. (2016). In addition, the configuration of the composited RUCs model looks for maximise boundary effects given that the distance between the vertical cracks of two consecutive RUCs is minimal.

Figure B2 shows a negligible discrepancy between numerical results for the models composed by one and four RUCs. These results validate the consideration of all the

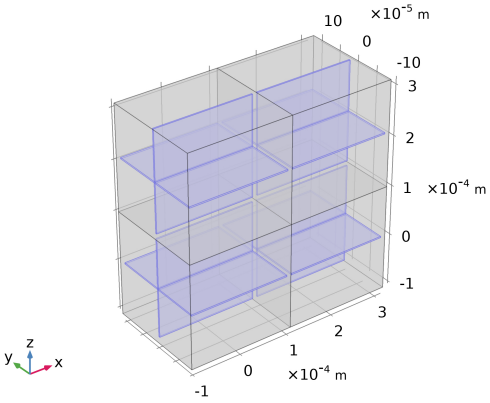

Figure B1. Model composed by four RUCs as the one presented in Figure 1 having two planar cracks with 2.7 μm of aperture.

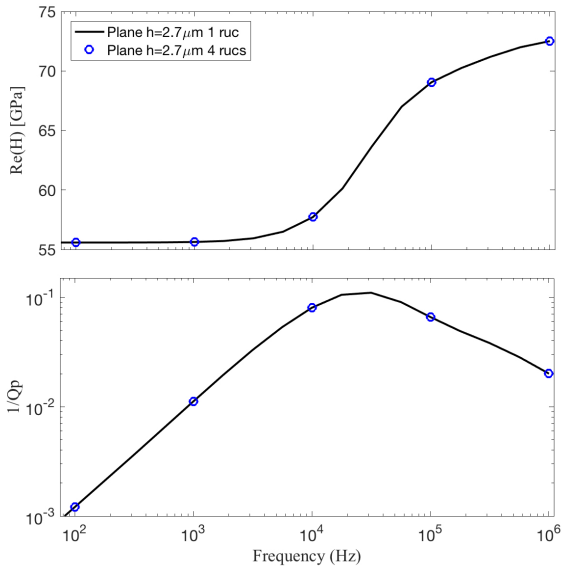

Figure B2. Real part of the P-wave modulus Re(H) and attenuation 1/Qp as functions of frequency for two models composed by one and four RUCs (as the one presented in Figure B1) having planar cracks with 2.7 μm of aperture.

numerical models presented in this work as REVs. Moreover, it verifies the fact that no considerable boundary effects are affecting the presented results.

Appendix C Hydraulic aperture

As part of our analysis, we compute the effective hydraulic aperture of the different cracks considered in this work. This allows us to interpret the seismic responses in terms of hydraulic properties of the cracks. We combine the cubic law and Darcy's law to obtain the hydraulic aperture (h_H) of our crack models (Jaeger et al., 2007),

$$h_H^3 = -\frac{Q_y 12\eta}{w\nabla p_y} \tag{C1}$$

where Q_y and ∇p_y are the volumetric flux and the fluid pressure gradient for the horizontal crack, respectively, in the fluid flow direction (i.e., y-direction) and w is the crack length in the horizontal direction normal to the fluid flow (i.e., x-direction). To obtain Q_y, we solve Stokes equations (neglecting inertial terms), using the finite element software COMSOL Multiphisics, for laminar incompressible flow within a horizontal crack. This test is performed in time domain and the fluid flow is stationary. The numerical estimation of the hydraulic aperture of a crack is obtained by applying a constant fluid pressure gradient ∇p_y between two opposite boundaries of a single crack. We measure Q_y at the crack boundary having the lowest fluid pressure. Unlike the numerical test previously described, there is no solid deformation in this test. Additionally, no slip boundary conditions are applied to the crack walls. Finally, we use Eq. C1 to obtain the crack hydraulic aperture.

Acknowledgments

This research has been supported by the Swiss National Science Foundation (grant no. 172691). We thank Holger Steeb for insightful discussions and Santiago G. Solazzi and J. Germán Rubino for useful suggestions. The data for this paper are available online (at http://doi.org/10.5281/zenodo.3573817).

References

Alkhimenkov, Y., Caspari, E., Gurevich, B., Barbosa, N. D., Glubokovskikh, S., Hunziker, J., & Quintal, B. (2020). Frequency-dependent attenuation and dispersion caused by squirt flow: Three-dimensional numerical study. *Geophysics*, *0*(0), 1-71. doi: 10.1190/geo2019-0519.1

Andrä, H., Combaret, N., Dvorkin, J., Glatt, E., Han, J., Kabel, M., ... Zhan, X. (2013). Digital rock physics benchmarks - part i: Imaging and segmentation. *Comput. Geosci.*, *50*, 25 - 32. (Benchmark problems, datasets and methodologies for the computational geosciences) doi: https://doi.org/10.1016/j.cageo.2012.09.005

Arena, A., Piane, C. D., & Sarout, J. (2014). A new computational approach to cracks quantification from 2d image analysis: Application to micro-cracks description in rocks. *Comput. Geosci.*, *66*, 106 - 120. doi: https://doi.org/10.1016/j.cageo.2014.01.007

Beran, M. J. (1968). Statistical continuum theories. *American Journal of Physics*, *36*(10), 923-923. doi: 10.1119/1.1974326

Borgomano, J. V. M., Pimienta, L. X., Fortin, J., & Guguen, Y. (2019). Seismic dispersion and attenuation in fluid-saturated carbonate rocks: Effect of microstructure and pressure. *Journal of Geophysical Research: Solid Earth*, *124*. doi: 10.1029/2019JB018434

Caspari, E., Gurevich, B., & Müller, T. M. (2013). Frequency-dependent effective hydraulic conductivity of strongly heterogeneous media. *Phys. Rev. E*, *88*, 042119. doi: 10.1103/PhysRevE.88.042119

Chapman, M., Zatsepin, S., & Crampin, S. (2002, 11). Derivation of a microstructural poroelastic model. *Geophysical Journal International*, *151*, 427-451. doi: 10.1046/j.1365-246X.2002.01769.x

Chapman, S., Borgomano, J. V. M., Yin, H., Fortin, J., & Quintal, B. (2019). Forced oscillation measurements of seismic wave attenuation and stiffness moduli dispersion in glycerine-saturated berea sandstone. *Geophysical Prospecting*, *67*(4), 956-968. doi: 10.1111/1365-2478.12710

Dagan, G. (1982). Analysis of flow through heterogeneous random aquifers: 2. unsteady flow in confined formations. *Water Resources Research*, *18*(5), 1571-1585. doi: 10.1029/WR018i005p01571

Das, V., Mukerji, T., & Mavko, G. (2019). Numerical simulation of coupled fluid-

solid interaction at the pore scale: A digital rock-physics technology. *Geophysics*, *84*(4), WA71-WA81. doi: 10.1190/geo2018-0488.1

Delle Piane, C., Arena, A., Sarout, J., Esteban, L., & Cazes, E. (2015). Microcrack enhanced permeability in tight rocks: An experimental and microstructural study. *Tectonophysics*, *665*, 149 - 156. doi: https://doi.org/10.1016/j.tecto.2015.10.001

Dvorkin, J., Derzhi, N., Diaz, E., & Fang, Q. (2011). Relevance of computational rock physics. *Geophysics*, *76*(5), E141-E153. doi: 10.1190/geo2010-0352.1

Dvorkin, J., Mavko, G., & Nur, A. (1995). Squirt flow in fully saturated rocks. *Geophysics*, *60*(1), 97–107.

Gassmann, F. (1951). Über die Elastizität poröser Medien. *Vierteljahresschr. Naturforsch. Ges. Zürich*, *96*, 1–23.

Guo, J., Rubino, J. G., Barbosa, N. D., Glubokovskikh, S., & Gurevich, B. (2018). Seismic dispersion and attenuation in saturated porous rocks with aligned fractures of finite thickness: Theory and numerical simulations ? part 1: P-wave perpendicular to the fracture plane. *Geophysics*, *83*(1), WA49-WA62. doi: 10.1190/geo2017-0065.1

Gurevich, B., Makarynska, D., de Paula, O. B., & Pervukhina, M. (2010). A simple model for squirt-flow dispersion and attenuation in fluid-saturated granular rocks. *Geophysics*, *75*(6), N109-N120. doi: 10.1190/1.3509782

Hudson, J. A., & Liu, E. (1999). Effective elastic properties of heavily faulted structures. *Geophysics*, *64*(2), 479-485. doi: 10.1190/1.1444553

Jaeger, J., G W Cook, N., & Zimmerman, R. (2007, 01). Fundamental of rock mechanics.. doi: 10.1017/CBO9780511735349

Jänicke, R., Quintal, B., & Steeb, H. (2015). Numerical homogenization of mesoscopic loss in poroelastic media. *Eur. J. Mech. A Solids*, *49*, 382-395.

Kachanov, M., & Mishakin, V. (2019). On crack density, crack porosity, and the possibility to interrelate them. *International Journal of Engineering Science*, *142*, 185 - 189. doi: https://doi.org/10.1016/j.ijengsci.2019.06.010

Klimentos, T. (1995). Attenuation of p? and s?waves as a method of distinguishing gas and condensate from oil and water. *GEOPHYSICS*, *60*(2), 447-458. doi: 10.1190/1.1443782

Lakes, R. (2009). *Viscoelastic materials*. Cambridge University Press. doi: 10.1017/CBO9780511626722

Lissa, S., Barbosa, N. D., Rubino, J. G., & Quintal, B. (2019). Seismic attenuation and dispersion in poroelastic media with fractures of variable aperture distributions. *Solid Earth*, *10*(4), 1321–1336. doi: 10.5194/se-10-1321-2019

Madonna, C., Quintal, B., Frehner, M., Almqvist, B. S. G., Tisato, N., Pistone, M., ... Saenger, E. H. (2013). Synchrotron-based x-ray tomographic microscopy for rock physics investigations. *Geophysics*, *78*(1), D53-D64. doi: 10.1190/geo2012-0113.1

Mavko, G., & Jizba, D. (1991). Estimating grain-scale fluid effects on velocity dispersion in rocks. *Geophysics*, *56*(12), 1940-1949. doi: 10.1190/1.1443005

Mavko, G., Mukerji, T., & Dvorkin, J. (2009). *The rock physics handbook: Tools for seismic analysis of porous media*. Cambridge University Press.

Metz, B., Davidson, O., de Coninck, H., Loos, M., & Meyer, L. (2005). Ipcc special report on carbon dioxide capture and storage. *Cambridge University Press*, 431.

Milani, M., Rubino, J. G., Müller, T. M., Quintal, B., Caspari, E., & Holliger, K. (2016). Representative elementary volumes for evaluating effective seismic properties of heterogeneous poroelastic media. *Geophysics*, *81*, D21–D33. doi: 10.1190/GEO2015-0173.1

Müller, T. M., Gurevich, B., & Lebedev, M. (2010). Seismic wave attenuation and dispersion resulting from wave-induced flow in porous rocks - a review. *Geophysics*, *75*, 147-163. doi: 10.1190/1.3463417

Murphy, W. F., Winkler, K. W., & Kleinberg, R. L. (1986). Acoustic relaxation in sedimentary rocks: Dependence on grain contacts and fluid saturation. *Geophysics*, *51*(3), 757-766. doi: 10.1190/1.1442128

Nolte, D. D., & Pyrak-Nolte, L. J. (1991, Nov). Stratified continuum percolation: Scaling geometry of hierarchical cascades. *Phys. Rev. A*, *44*, 6320 - 6333. doi: 10.1103/PhysRevA.44.6320

O'Connell, R. J., & Budiansky, B. (1977). Viscoelastic properties of fluid-saturated cracked solids. *Journal of Geophysical Research (1896-1977)*, *82*(36), 5719-5735. doi: 10.1029/JB082i036p05719

O'Connell, R. J., & Budiansky, B. (1978). Measures of dissipation in viscoelastic media. *Geophys. Res. Lett.*, *5*, 5–8. doi: 10.1029/GL005i001p00005

Pimienta, L., Fortin, J., & Guguen, Y. (2015). Experimental study of young's modulus dispersion and attenuation in fully saturated sandstones. *Geophysics*, *80*(5), L57-L72. doi: 10.1190/geo2014-0532.1

Pride, S. R., Berryman, J. G., & Harris, J. M. (2004). Seismic attenuation due to wave-induced flow. *J. Geophys. Res.*, *109,* B01201. doi: 10.1029/2003JB002639

Pyrak-Nolte, L., Myer, L., Cook, N., & Witherspoon, P. (1987, 1). Hydraulic and mechanical properties of natural fractures in low-permeability rock.

Quintal, B., Caspari, E., Holliger, K., & Steeb, H. (2019). Numerically quantifying energy loss caused by squirt flow. *Geophysical Prospecting*, *67*(8), 2196-2212. doi: 10.1111/1365-2478.12832

Quintal, B., Rubino, J. G., Caspari, E., & Holliger, K. (2016). A simple hydromechanical approach for simulating squirt-type flow. *Geophysics*, *81*(4), D335-D344. doi: 10.1190/geo2015-0383.1

Rapoport, M. B., Rapoport, L. I., & Ryjkov, V. I. (2004). Direct detection of oil and gas fields based on seismic inelasticity effect. *The Leading Edge*, *23*(3), 276-278. doi: 10.1190/1.1690901

Rubino, J. g., Caspari, E., Müller, T. M., Milani, M., Barbosa, N. D., & Holliger, K. (2016). Numerical upscaling in 2-d heterogeneous poroelastic rocks: Anisotropic attenuation and dispersion of seismic waves. *J. Geophys. Res.*, *121*(9), 6698–6721.

Saenger, E. H., Enzmann, F., Keehm, Y., & Steeb, H. (2011). Digital rock physics: Effect of fluid viscosity on effective elastic properties. *Journal of Applied Geophysics*, *74*(4), 236 - 241. doi: https://doi.org/10.1016/j.jappgeo.2011.06.001

Saenger, E. H., Lebedev, M., Uribe, D., Osorno, M., Vialle, S., Duda, M., ... Steeb, H. (2016). Analysis of high-resolution x-ray computed tomography images of bentheim sandstone under elevated confining pressures. *Geophysical Prospecting*, *64*(4), 848-859. doi: 10.1111/1365-2478.12400

Sanchez-Vila, X., Guadagnini, A., & Carrera, J. (2006). Representative hydraulic conductivities in saturated groundwater flow. *Reviews of Geophysics*, *44*(3). doi: 10.1029/2005RG000169

Shapiro, S. A. (2003). Elastic piezosensitivity of porous and fractured rocks. *Geophysics*, *68*(2), 482-486. doi: 10.1190/1.1567215

Silliman, S. E. (1989). An interpretation of the difference between aperture estimates derived from hydraulic and tracer tests in a single fracture. *Water Resources Research*, *25*(10), 2275-2283. doi: 10.1029/WR025i010p02275

Solazzi, S. G., Rubino, J. G., Müller, T. M., Milani, M., Guarracino, L., & Holliger, K. (2016). An energy-based approach to estimate seismic attenuation due to wave-induced fluid flow in heterogeneous poroelastic media. *Geophys. J. Int.*, *207(2)*, 823–832.

Subramaniyan, S., Quintal, B., Madonna, C., & Saenger, E. H. (2015). Laboratory-based seismic attenuation in fontainebleau sandstone: Evidence of squirt flow. *J. Geophys. Res. Solid Earth*, *120*(11), 7526–7535.

Tester, J. W., Anderson, B. J., Batchelor, A. S., Blackwell, D. D., DiPippo, R.,

Drake, E. M., ... Richards, M. (2007). Impact of enhanced geothermal systems on us energy supply in the twenty-first century. *Philosophical Transactions of the Royal Society A: Mathematical, Physical and Engineering Sciences*, *365*(1853), 1057-1094. doi: 10.1098/rsta.2006.1964

Zhang, Y., & Toksöz, N. (2012, 08). Computation of dynamic seismic responses to viscous fluid of digitized three-dimensional berea sandstones with a coupled finite-difference method. *The Journal of the Acoustical Society of America*, *132*, 630-40. doi: 10.1121/1.4733545

Zimmerman, R., & Main, I. (2004). Hydromechanical behavior of fractured rocks. *InGeo*, *89*, 363–422.